

Identification of three new ultraluminous X-ray sources in NGC 4631 and NGC 1097: Evidence for stellar-mass black holes

Sinan Allak¹*, Aysun Akyuz^{2,3}, Yasemin Aladag², Lorenzo Ducci¹, and Andrea Santangelo¹

¹ Institut für Astronomie und Astrophysik, Sand 1, 72076 Tübingen, Germany
e-mail: sinan.allak@uni-tuebingen.de

² Department of Physics, University of Çukurova, 01330, Adana, Türkiye

³ Space Science and Solar Energy Research and Application Center (UZAYMER), University of Çukurova, 01330, Adana, Türkiye

Received September 15, 2025; accepted .., ..

ABSTRACT

Context.

Aims. Recent observations of galaxies continue to reveal new ultraluminous X-ray sources (ULXs), thereby increasing their known population. This growing sample provides improved statistics that are essential for advancing our understanding of ULX properties and their nature.

Methods. Our objective was to study the source populations using published *Chandra*, *XMM-Newton*, and *Swift*/XRT observations to identify new ULXs. In particular, we focused on investigating their X-ray and optical properties to constrain the nature of the compact objects and donor stars.

Results. We analyzed archival X-ray observations spanning 2000 to 2025 for NGC 4631 and NGC 1097 to study their ULX populations. We performed spectral fitting for sources with sufficient counts using absorbed power-law and diskbb models to determine their physical properties. We conducted variability analyses, including hardness-intensity diagrams and light curves, to assess both short- and long-term variability. Additionally, we used optical color-magnitude diagrams and near-infrared (NIR) spectral energy distributions (SEDs) to identify and characterize possible donor stars.

Conclusions. In NGC 4631, we identify two new transient ULXs, X-6 and X-7, whose X-ray count rates vary by more than an order of magnitude. The $L_X \propto T^4$ relation obtained from the diskbb fits provides strong evidence that NGC 4631 X-6 is powered by a stellar-mass black hole (BH) accreting via a standard disk. The optical sources within the X-6 and X-7 X-ray error circles are candidate optical counterparts, suggesting that these systems are candidate high-mass X-ray binaries. In NGC 1097, we report the discovery of a new transient ULX, designated ULX-3, which exhibits variations in X-ray luminosity (L_X) by a factor of about 30. For ULX-3, we detect spectral state transitions, which may indicate a compact object consistent with either a stellar-mass BH or a neutron star. Moreover, we identify a unique optical and NIR counterpart: while the optical emission is variable, the NIR emission remains stable. The NIR counterpart of ULX-3 shows an SED consistent with a blackbody temperature of ~ 3300 K, which lies within the expected range for red supergiants with a stellar radius of $\sim 200R_\odot$.

Key words. NGC 4631 – NGC 1097 – accretion discs – X-rays: binaries – stars: black holes

1. Introduction

Ultraluminous X-ray sources (ULXs) are the most extreme subclass of X-ray binaries (XRBs), appearing as off-nuclear point sources exhibiting $L_X > 2 \times 10^{39}$ erg s⁻¹ (Kaaret et al. 2017; Fabrika et al. 2021; King et al. 2023; Pinto & Walton 2023). To account for their ultraluminosities, recent studies increasingly support the view that the majority of ULXs are powered by stellar-mass compact objects undergoing super-Eddington accretion (King et al. (2023) and references therein), rather than by sub-Eddington accretion onto intermediate-mass black holes (Heinzeller et al. 2006; Brightman et al. 2019; Greene 2022). Within this framework, the accreting compact object is generally inferred to be either a black hole (BH) or a neutron star (NS).

Coherent pulsations have been detected in several ULXs, confirming them as pulsating NS ULXs (PULXs), primarily through observations by *XMM-Newton* and *NuSTAR* (Bachetti et al. 2014; Motch et al. 2014; Israel et al. 2017; Carpano et al.

2018). Moreover, the observation of cyclotron resonance scattering features in the X-ray spectrum of a ULX implies the presence of an NS candidate (Mushtukov et al. 2017; Pinto et al. 2020). In addition, several ULXs, including some identified as PULXs, show transient behavior, whereas most remain persistently bright in the X-ray band over long timescales. Repeated observations of nearby galaxies with *Chandra* and *XMM-Newton* have contributed to a growing number of ULXs, particularly those exhibiting transient behavior (van Haafken et al. 2019; Earnshaw et al. 2020; Walton et al. 2021; Robba et al. 2022; Roberts et al. 2023; Brightman et al. 2023; Allak 2023).

Several ULXs also show clear evidence of recurrent spectral state transitions, evolving from hard to soft regimes over time, as revealed by high-cadence and long-term studies. In particular, Holmberg II X1 and NGC 5204 X1 show a cyclical evolution through the states of hard ultra-luminous (HUL), soft ultra-luminous (SUL), and supersoft ultra-luminous (SSUL), likely driven by variations in accretion rate and changes in funnel geometry caused by radiation-driven winds (Gúrpide et al. 2021b; Mondal et al. 2021). A recent study by Majumder et al. (2025) analyzed the long-term evolution of several ULXs with candi-

* Corresponding author: e-mail: sinan.allak@uni-tuebingen.de

date BH accretors using *XMM-Newton*, revealing diverse spectrotemporal behaviors and correlations between disk luminosity (L_{disc}) and inner-disk temperature (T_{col}). The authors argue that these correlations are indicative of possible spectral states or transitions between standard thin-disk and slim-disk configurations at different luminosities, supporting a two-component supercritical accretion framework regulated by the disk, corona, and radiation-driven winds. Numerous studies have sought to identify the optical counterparts of ULXs and clarify the origin of their emission (Tao et al. 2011; Soria et al. 2012; Gladstone et al. 2013; Vinokurov et al. 2018; Allak et al. 2022; Guo et al. 2023; Allak & Akyuz 2025). However, determining the precise contributions remains challenging, as the emission may originate from the donor star's photosphere, the accretion disk, or a combination of both (Tao et al. 2011; Fabrika et al. 2015; Allak et al. 2022). In rare cases, spectral signatures such as stellar absorption lines allow clear donor identification, as seen in NGC 7793 P13, where a B9Ia supergiant was confirmed (Motch et al. 2014). Optical variability has also been observed in several ULXs, such as ULX-4 and ULX-8 (both in M51) and NGC 1313 X-2, suggesting accretion disc-dominated emission in these systems (Liu et al. 2009; Allak 2022). Optical counterparts of ULXs are generally faint ($m_V > 20$ mag) and frequently obscured by surrounding stellar populations or interstellar material, which complicates their detection and interpretation. In contrast, infrared (IR) observations, particularly in the NIR range, are less affected by dust extinction and provide valuable insights into the nature of donor stars and the circumstellar environments of ULXs. Several ULXs have reported NIR magnitudes consistent with red supergiants (RSGs) Heida et al. 2014; Lau et al. 2019; Dudik et al. 2016, and spectroscopic analyses suggest RSG-like donors in some cases (Heida et al. 2016). Mid-IR emission is also attributed to either circumstellar dust or jets (Dudik et al. 2016; Lau et al. 2019; Allak 2023). NGC 4631, also known as the Whale Galaxy, is a barred spiral galaxy that exhibits starburst activity. It is located in the constellation Canes Venatici, approximately 7.6 Mpc away ($1'' = 34$ pc) (Soria & Ghosh 2009). Several studies have explored the ULX population in NGC 4631, revealing a range of accretion processes. Carpano et al. (2007) reported the discovery of a supersoft ULX that exhibits a 4-hour periodic modulation based on *XMM-Newton* data. This supersoft ULX is unlikely to be explained by the standard white dwarf scenario without extreme beaming. It has been suggested that it may instead be a stellar-mass BH accreting at super-Eddington rates, with the modulation resulting from either a companion eclipse or a warped accretion disk.

Furthermore, using archival data from *XMM-Newton*, *Chandra*, and *ROSAT*, Soria & Ghosh (2009) reanalyzed the five brightest X-ray sources in NGC 4631, identifying four (X1, X2, X4, and X5) as ULXs. Among these, X1—previously described as a supersoft source by Carpano et al. (2007)—has been proposed to represent an extreme subclass of supersoft sources, powered by transient super-Eddington outbursts driven by non-steady nuclear burning on the surface of a massive white dwarf. The other sources displayed spectral properties consistent with stellar-mass BHs accreting at super-Eddington rates. Moreover, Ducci et al. (2025) report the discovery of a new transient pulsar ULX in NGC 4631, designated X-8, with a spin period of 9.67 s and a very high spin-up rate, $\dot{P} \sim -9.6 \times 10^{-8}$ s/s. Guo et al. (2023) studied the optical counterparts of ULXs in NGC 4631 using a broadband and narrowband imaging campaign with *Canada-France-Hawaii Telescope* (CFHT)/MegaCamm, aiming to detect bubble structures around the X-ray sources and examining their accretion proper-

ties. They analyzed the stellar surroundings of the sources via extinction-corrected color-magnitude diagrams and isochrone fitting. Their study reveals a highly asymmetric bubble nebula around X4, displaying distinct morphologies in $\text{H}\alpha$ and [O III] emission.

NGC 1097 ($D = 16.8$ Mpc, $1'' = 82$ pc; Liu 2011) is typically classified as a barred spiral (SBb) galaxy. It is also classified as a Seyfert 2 galaxy, which hosts an active galactic nucleus (AGN) powered by a central supermassive BH. Consequently, most studies of this galaxy have focused on constructing the SED of its nucleus using X-ray and multiwavelength observations (Nemmen et al. 2006). Observations with *Chandra* data further revealed two ULX sources, X2 and X3, in the galaxy, with model-estimated luminosities of 7×10^{39} erg s $^{-1}$ and 3×10^{39} erg s $^{-1}$, respectively (Liu 2011).

In this study, we investigate the nature of two newly identified ULX sources in NGC 4631, designated X-6 and X-7, and one ULX source in NGC 1097, designated ULX-3. To achieve this, we used archival data from multiple wavelengths, including X-ray observations from *Chandra*, *XMM-Newton*, and *Swift/XRT*, as well as optical data from the Hubble Space Telescope (HST). The precise positions of the ULX sources studied in both galaxies are shown on the *Chandra* images in Fig. 1. In addition, we analyzed infrared data from the James Webb Space Telescope (JWST) for the ULX in NGC 1097. The paper is organized as follows: Section 2 provides details of the observations. Section 3 describes the data reduction and analysis of X-ray and optical observations. Section 4 presents the results and discusses the properties of the ULXs. Finally, Section 5 summarizes the main findings of this study.

2. Observations

The NGC 4631 galaxy was observed with the *Chandra* ACIS-S instrument over 12 observations between 2000 and 2023. Archival observations of the galaxy also include data from *XMM-Newton* taken in 2002, two observations in 2021, and one in 2025. The *HST* observed the galaxy in 2003 and 2014 using the Advanced Camera for Surveys/Wide Field Channel (ACS/WFC). NGC 4631 was also observed 24 times by *Swift/XRT* between 2013 and 2021, with individual exposure times ranging from 128 to 7369 s. In addition, between 8 June 2024 and 9 January 2025, the JWST/Mid-Infrared Instrument (MIRI) observed NGC 4631 using the F1130W, F1500W, F1800W, F560W, and F770W filters. We did not use the JWST data in this study because their spatial resolution (0.11 arcsec/pixel ~ 4 pc/pixel) was insufficient to resolve the counterparts of X-6 and X-7.

The *Chandra* ACIS-S instrument observed NGC 1097 in six separate sessions between 2001 and 2025. The initial observation took place on January 28, 2001, followed by five observations in 2025 (three on 21 May, two on 31 May). The galaxy also has *XMM-Newton* data from an observation conducted on 22 December 2023. In addition, the JWST/NIRCam (Near-Infrared Camera) and MIRI (Mid-Infrared Instrument) instruments observed NGC 1097 with multiple filters between 27 December 2023 and 29 September 2024. The *HST* also observed the galaxy on multiple occasions using different optical filters between 5 June 2004 and 20 August 2025. For *Swift/XRT*, 86 photon counting (PC) mode observations associated with Target IDs 00045597 and 00036582 were carried out between 2007 and 2025. Table A.1 provides additional details on the observations of NGC 4631 and NGC 1097.

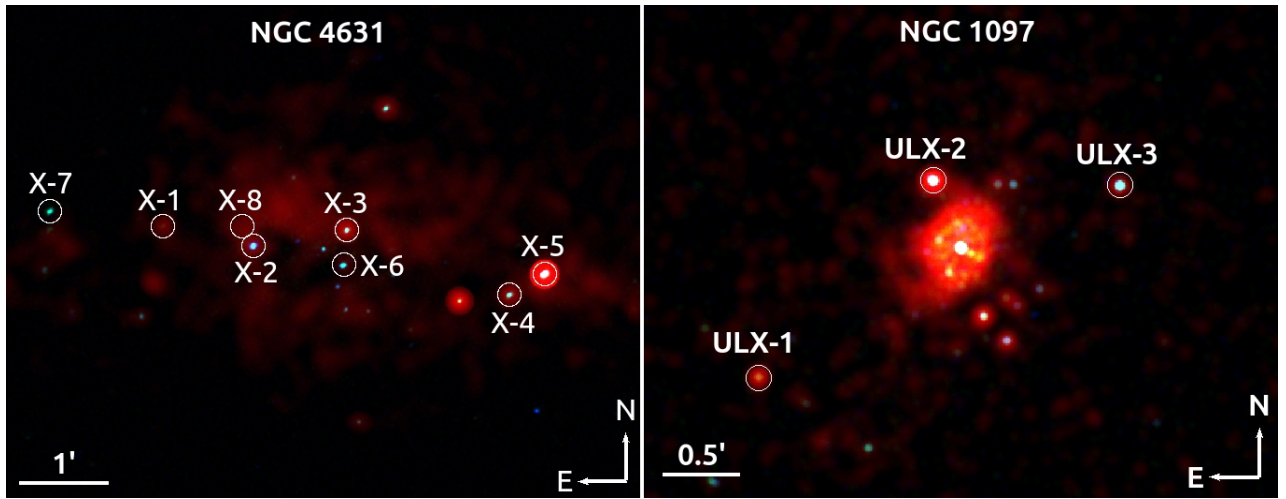


Fig. 1. X-ray color-stacked *Chandra* images of the galaxies NGC 4631 (left) and NGC 1097 (right). The energy ranges used for the red, green, and blue colors in both images are 0.5–1.2, 1.2–2, and 2–8 keV, respectively. The positions of the ULXs are indicated with solid white circles.

3. X-ray and multiwavelength data reduction and analysis

3.1. X-ray energy spectra

We processed the *Chandra* ACIS-S datasets using *Chandra* Interactive Analysis of Observations (CIAO) (Fruscione et al. 2006) and calibration files from the Calibration Database (CALDB) version 4.11, generating level 2 event files using the *chandra_repro* script available in *CIAO*. Using the *wavdetect* tool in *CIAO*, we identified X-ray sources and applied wavelet scales of 2, 4, 8, and 16 pixels with a detection threshold set to 10^{-6} . The positions of the sources newly classified as ULXs in this study, based on *Chandra* observations, are: NGC 4631 X-6 at $\alpha = 12^{\text{h}}42^{\text{m}}06\rlap{.}^{\text{s}}38$, $\delta = +32^{\circ}32'22\rlap{.}^{\text{s}}95$; NGC 4631 X-7 at $\alpha = 12^{\text{h}}42^{\text{m}}22\rlap{.}^{\text{s}}05$, $\delta = +32^{\circ}32'59\rlap{.}^{\text{s}}32$; and NGC 1097 ULX-3 at $\alpha = 02^{\text{h}}46^{\text{m}}14\rlap{.}^{\text{s}}16$, $\delta = -30^{\circ}16'04\rlap{.}^{\text{s}}65$.

We derived spectral data and light curves with *specextract* and *dmextract*, respectively. For *Chandra* observations, we extracted the source counts using a circular region with a radius of $4''$. We used two methods to estimate the background: (i) a nearby circular region with a radius of $8''$, free of point sources, and (ii) an annulus centered on the ULX with inner and outer radii of $6''$ and $10''$, respectively. Both approaches yield consistent net count rates within uncertainties. We analyzed *XMM-Newton* European Photon Imaging Camera (EPIC) observations using the science analysis system (SAS)¹ v22.0. Response files (RMFs and ARFs) for the EPIC-pn and MOS (Metal Oxide Semiconductor detectors) were generated using the *rmfgen* and *arfgen* tasks, respectively. The event selection criteria included $\text{PATTERN} \leq 12$ for European Photon Imaging Camera – Metal Oxide Semiconductor (EPIC-MOS) and $\text{PATTERN} \leq 4$ for PN, with $\text{FLAG}=0$ applied in both cases. We extracted source and background events from circular regions with radii of $15''$ and $30''$, respectively, using the *evselect* task. Because NGC 4631 X-6 and NGC 1097 ULX-3 fall into the chip gap of the PN detector on *XMM-Newton*, we used data from the MOS detectors only. We used FTOOLS *grppha* to group the source energy spectra. For the *XMM-Newton* MOS data, we grouped the spectra with at least 15–20 counts per energy bin to enable χ^2 spectral fitting. For *Chandra* observations, the spectra were grouped

with 5–10 counts per energy bin, using C-statistics suitable for Poisson-distributed data. We performed all spectral fits using XSPEC (Arnaud 1996), covering 0.5–8 keV (*Chandra*) and 0.3–10 keV (*XMM-Newton*), to determine the best-fitting models. In addition, due to limited photon statistics in some *Chandra* observations and considering variability timescales, we combined spectra from closely spaced observations to improve the data's statistical quality and obtain the best spectral fits.

For NGC 4631 ULXs, two-component models did not provide a statistically significant improvement over single-component models. Therefore, we adopted single-component models, either a power-law or a diskbb model combined with two absorption components (tbabs). We used two tbabs components: one fixed at the Galactic hydrogen column density ($N_{\text{H}} = 0.013 \times 10^{22} \text{ cm}^{-2}$) to account for Galactic absorption (Dickey & Lockman 1990), and the other free to model intrinsic absorption. We initially derived intrinsic N_{H} values from the spectral fits and interpreted the observed variations as more likely statistical than physical. To avoid these fluctuations mimicking flux changes, we repeated the fits with intrinsic N_{H} fixed to the average of the initial values obtained. Intrinsic absorption variability in ULXs remains debated, with reports of both variable N_{H} (e.g., Kajava & Poutanen 2009) and more stable absorption properties (e.g., Gúrpide et al. 2021a). For NGC 1097 ULX-3, we performed spectral modeling using only the *XMM-Newton* observation, because the *Chandra* observations had insufficient photon counts. with the spectrum best fit by a combined power-law plus bbody model. We provide detailed model parameters for the ULXs, along with the absorbed flux estimated using the *cflux* convolution model in XSPEC, in Tables 1, 2, and 3 for X-6, X-7, and ULX-3, respectively. Figures 2 and 3 show the corresponding energy spectra.

3.2. Short- and long-term X-ray variability

To investigate the short-term X-ray variability of the three newly identified ULXs, we extracted light curves for all available *Chandra* data in the 0.5–8 keV band and from *XMM-Newton* data in the 0.3–10 keV band. The analysis was performed using time bins of 100, 500, and 1000 seconds. We used the CIAO and SAS tools *dmextract* and *evselect* to background-extract light curves. For the absolute timing analysis, we applied the

¹ <https://www.cosmos.esa.int/web/xmm-newton/sas>

Table 1. X-ray spectral parameters of NGC 4631 X-6 in *Chandra* and *XMM-Newton* observations.

Data label	Net Rate (10^{-3} counts/s)	N_H (10^{22} cm^{-2})	Γ/Γ_{in} (/keV)	Γ^*/Γ_{in}^* (/keV)	C_{stat}/dof	F_x ($10^{-13} \text{ erg cm}^{-2} \text{ s}^{-1}$)	L_x ($10^{39} \text{ erg s}^{-1}$)	F_x^* ($10^{-13} \text{ erg cm}^{-2} \text{ s}^{-1}$)	L_x^* ($10^{39} \text{ erg s}^{-1}$)
C1	>0.08								
<i>tbabs*tbabs*power-law</i>									
C2	17.64 ± 0.78	$1.76^{+0.16}_{-0.21}$	$2.69^{+0.08}_{-0.07}$	$2.07^{+0.07}_{-0.07}$	21.56/28 ^b	$3.07^{+0.30}_{-0.29}$	$7.78^{+0.58}_{-0.58}$	$3.26^{+0.29}_{-0.29}$	$4.12^{+0.31}_{-0.31}$
C3	7.93 ± 0.59	$0.92^{+0.19}_{-0.21}$	$2.32^{+0.13}_{-0.13}$	$2.31^{+0.13}_{-0.13}$	27.48/29	$1.48^{+0.29}_{-0.23}$	$2.16^{+0.27}_{-0.27}$	$1.50^{+0.24}_{-0.24}$	$2.12^{+0.27}_{-0.27}$
C4	9.75 ± 0.73	$2.06^{+0.23}_{-0.23}$	$3.38^{+0.14}_{-0.14}$	$2.33^{+0.14}_{-0.14}$	21.99/30	$1.65^{+0.31}_{-0.25}$	$8.89^{+0.75}_{-0.75}$	$1.88^{+0.32}_{-0.27}$	$4.75^{+0.61}_{-0.56}$
$C_{combine}1$	9.06 ± 0.47	$1.41^{+0.15}_{-0.14}$	$2.78^{+0.09}_{-0.10}$	$2.37^{+0.13}_{-0.13}$	58.47/60	$1.55^{+0.19}_{-0.17}$	$3.76^{+0.33}_{-0.32}$	$1.64^{+0.18}_{-0.16}$	$2.07^{+0.19}_{-0.19}$
C5	8.25 ± 0.64	$1.35^{+0.28}_{-0.26}$	$1.93^{+0.12}_{-0.12}$	$1.59^{+0.16}_{-0.12}$	35.92/29	$1.89^{+0.44}_{-0.33}$	$2.53^{+0.33}_{-0.31}$	$2.00^{+0.37}_{-0.31}$	$2.07^{+0.28}_{-0.26}$
C6	9.63 ± 0.81	$0.60^{+0.28}_{-0.25}$	$1.83^{+0.15}_{-0.14}$	$2.06^{+0.15}_{-0.14}$	32.27/22	$2.29^{+0.87}_{-0.87}$	$2.29^{+0.33}_{-0.30}$	$2.18^{+0.43}_{-0.35}$	$2.68^{+0.39}_{-0.35}$
C7	9.69 ± 0.81	$2.10^{+0.23}_{-0.29}$	$2.71^{+0.14}_{-0.13}$	$1.83^{+0.14}_{-0.13}$	20.52/23	$1.68^{+0.42}_{-0.30}$	$5.26^{+0.69}_{-0.51}$	$2.14^{+0.41}_{-0.34}$	$2.36^{+0.35}_{-0.31}$
C8	4.59 ± 0.39	$1.09^{+0.23}_{-0.21}$	$2.65^{+0.16}_{-0.17}$	$2.47^{+0.16}_{-0.15}$	32.46/23	$0.73^{+0.20}_{-0.14}$	$1.44^{+0.51}_{-0.20}$	$0.77^{+0.15}_{-0.12}$	$1.21^{+0.18}_{-0.16}$
$C_{combine}2$	2.49 ± 0.20	$1.67^{+0.20}_{-0.18}$	$3.65^{+0.17}_{-0.16}$	$2.80^{+0.17}_{-0.16}$	22.76/26	$0.39^{+0.08}_{-0.06}$	$2.47^{+0.34}_{-0.31}$	$0.44^{+0.08}_{-0.06}$	$0.89^{+0.12}_{-0.11}$
<i>tbabs*tbabs*diskbb</i>									
C2		$0.84^{+0.16}_{-0.14}$	$1.21^{+0.02}_{-0.02}$	$1.39^{+0.03}_{-0.03}$	17.62/28 ^b	$2.94^{+0.29}_{-0.28}$	$3.07^{+0.23}_{-0.23}$	$3.05^{+0.28}_{-0.28}$	$2.70^{+0.20}_{-0.20}$
C3		$0.25^{+0.19}_{-0.21}$	$1.39^{+0.03}_{-0.03}$	$1.24^{+0.04}_{-0.04}$	27.22/29	$1.47^{+0.33}_{-0.23}$	$1.14^{+0.14}_{-0.14}$	$1.40^{+0.23}_{-0.19}$	$1.25^{+0.16}_{-0.15}$
C4		$1.01^{+0.22}_{-0.21}$	$0.89^{+0.03}_{-0.03}$	$1.09^{+0.03}_{-0.03}$	23.44/30	$1.55^{+0.27}_{-0.22}$	$1.93^{+0.25}_{-0.23}$	$1.65^{+0.27}_{-0.23}$	$1.52^{+0.19}_{-0.18}$
$C_{combine}1$		$0.57^{+0.14}_{-0.14}$	$1.13^{+0.02}_{-0.02}$	$1.17^{+0.03}_{-0.03}$	59/60	$1.49^{+0.18}_{-0.16}$	$1.41^{+0.13}_{-0.13}$	$1.51^{+0.16}_{-0.15}$	$1.37^{+0.12}_{-0.12}$
C5		$0.77^{+0.28}_{-0.28}$	$1.69^{+0.06}_{-0.06}$	$2.01^{+0.08}_{-0.08}$	36.04/29	$1.75^{+0.46}_{-0.31}$	$1.64^{+0.22}_{-0.20}$	$1.83^{+0.40}_{-0.30}$	$1.56^{+0.18}_{-0.18}$
C6		$0.11^{+0.25}_{-0.28}$	$1.70^{+0.06}_{-0.06}$	$1.39^{+0.05}_{-0.05}$	31.76/22	$2.24^{+0.57}_{-0.52}$	$1.57^{+0.23}_{-0.23}$	$1.98^{+0.42}_{-0.32}$	$1.72^{+0.23}_{-0.23}$
C7		$1.22^{+0.31}_{-0.29}$	$1.16^{+0.04}_{-0.04}$	$1.27^{+0.02}_{-0.02}$	17.82/23	$1.76^{+0.23}_{-0.19}$	$2.05^{+0.37}_{-0.36}$	$1.76^{+0.28}_{-0.26}$	$1.63^{+0.22}_{-0.22}$
C8		$0.45^{+0.23}_{-0.21}$	$1.04^{+0.04}_{-0.04}$	$1.02^{+0.04}_{-0.04}$	30.64/23	$0.67^{+0.12}_{-0.12}$	$0.63^{+0.09}_{-0.08}$	$0.67^{+0.13}_{-0.10}$	$0.64^{+0.09}_{-0.08}$
$C_{combine}2$		$0.81^{+0.20}_{-0.18}$	$0.73^{+0.02}_{-0.02}$	$0.83^{+0.03}_{-0.02}$	20.85/26	$0.36^{+0.05}_{-0.06}$	$0.50^{+0.07}_{-0.06}$	$0.38^{+0.06}_{-0.05}$	$0.40^{+0.05}_{-0.05}$
XM1	>2.74								
XM2	21.57 ± 0.93	$0.71^{+0.17}_{-0.22}$	$1.40^{+0.20}_{-0.24}$		34.53/33	$3.80^{+0.14}_{-0.16}$	$2.30^{+0.08}_{-0.10}$	-	-
XM3	>2.11								

Notes: The N_H of one tbabs component was fixed to the line-of-sight value of $0.013 \times 10^{22} \text{ cm}^{-2}$. The intrinsic N_H (second tbabs component) was left to free to vary; for the entries marked with (*), the intrinsic N_H was fixed at average values of $0.90 \times 10^{22} \text{ cm}^{-2}$ and $0.49 \times 10^{22} \text{ cm}^{-2}$ for the power-law and diskbb models, respectively. $C_{combine}1$ and $C_{combine}2$ correspond to combined observations C3–C4 and C9–C12, respectively. The count rate values for C9–C12 are $(1.68 \pm 0.38) \times 10^{-3}$, $(2.07 \pm 0.32) \times 10^{-3}$, $(2.42 \pm 0.35) \times 10^{-3}$, and $(2.57 \pm 0.44) \times 10^{-3}$, respectively. The superscript b. indicates that the corresponding spectral fits were performed using the χ^2/dof statistic. Absorbed fluxes were calculated in the 0.5–8 keV energy range, while unabsorbed luminosities were derived assuming a distance of 7.6 Mpc. Quoted uncertainties correspond to the 90% confidence level for each parameter

axbary task to the event file to correct the photon arrival times to the Solar System barycenter, thereby accounting for delays introduced by the orbital motion of the Earth and the *Chandra* spacecraft.

We applied the Lomb-Scargle periodogram (LS) and fast Fourier transform (FFT) methods to the light curves to search for periodic signals or variability. In the C2 observation of the NGC 4631 ULX X-6 light curve (Figure 4a), we detected a periodic variation at $P = 5120$ s (~ 1.42 hr; 2.6σ significance). This signal was identified using both the LS method and with XRONOS from the power density spectrum (Figure 4b). Figure 4c illustrates the folded light curve for this period. To study L_X variability, we constructed long-term light curves of X-6 and X-7 from available *Chandra* data. These luminosities were derived from the best-fit reduced C-stat values obtained in the spectral analysis (Tables 1 and 2). For NGC 1097 ULX-3, we constructed a long-term X-ray light curve using all available archival *Swift*/XRT PC mode observations, along with data from *Chandra* and *XMM-Newton*. We generated the *Swift*/XRT light curve using a custom Python script (*swiftdtools*) designed for *Swift*/XRT analysis. The source and background regions were circular, with radii of 30'' and 60'', respectively. We converted the resulting count rates to L_X (0.3–10 keV) using the spectral model parameters from Table 3 and the WebPIMMS tool. For *XMM-Newton*, we derived luminosities from MOS data based on our spectral modeling,

while for *Chandra* observations, we utilized the *srcflux* tool. We show the ULX-3 light curve in Figure 6 (left panel).

3.3. Spectral evolution and state transition

We investigated the spectral evolution of NGC 4631 X-6 and X-7 using *Chandra* observations, excluding non-detections. Soft (S), medium (M), and hard (H) bands were defined as 0.3–1.2 keV, 1.2–2 keV, and 2–8 keV, respectively, and the M/S and H/M hardness ratios (HR) were calculated. The temporal evolution of the hardness ratios is shown in the left panel of Figure 5, and the hardness–intensity diagram is shown in the right panel. When a band had insufficient counts, we adopted 3σ upper limits. To investigate potential spectral state transitions of NGC 1097 ULX-3, we constructed a hardness–intensity diagram (right panel of Figure 6), using count rates in the 0.3–1.5 keV (S) and 1.5–10 keV (H) bands. To account for differences in instrumental responses, we normalized the count rates from *Chandra* and *XMM-Newton* observations to those from *Swift*/XRT using WebPIMMS.

3.4. Optical and infrared photometry

For all drizzled HST/Wide Field Camera 3/Ultraviolet and Visible channel (WFC3/UVIS) and HST/Advanced Camera for Surveys/Wide Field Channel (ACS/WFC) images, we identified

Table 2. X-ray spectral parameters of NGC 4631 in the *Chandra* and *XMM-Newton* observations.

Data label	Net Rate (10^{-3} counts/s)	N_H (10^{22} cm^{-2})	Γ/T_{in} (/keV)	$C_{\text{stat/dof}}$	F_x ($10^{-13} \text{ erg cm}^{-2} \text{ s}^{-1}$)	L_x ($10^{39} \text{ erg s}^{-1}$)
<i>tbabs*tbabs*diskbb</i>						
C1	>0.20					
C2	6.56 ± 0.48	$1.25^{+0.20}_{-0.19}$	$0.60^{+0.01}_{-0.01}$	34.08/30	$0.88^{+0.13}_{-0.11}$	$1.78^{+0.22}_{-0.21}$
C3	7.72 ± 0.58	$0.66^{+0.21}_{-0.19}$	$0.95^{+0.03}_{-0.03}$	14.69/27	$1.09^{+0.22}_{-0.18}$	$1.16^{+0.15}_{-0.14}$
C4	6.19 ± 0.58	$0.17^{+0.20}_{-0.17}$	$0.87^{+0.03}_{-0.03}$	10.10/18	$0.93^{+0.18}_{-0.22}$	$0.75^{+0.12}_{-0.11}$
C5	8.55 ± 0.64	$0.91^{+0.20}_{-0.18}$	$0.69^{+0.02}_{-0.02}$	26.59/28	$1.01^{+0.17}_{-0.14}$	$1.61^{+0.21}_{-0.19}$
C6	7.75 ± 0.72	$0.14^{+0.23}_{-0.14}$	$0.78^{+0.03}_{-0.03}$	12.44/17	$1.05^{+0.32}_{-0.29}$	$0.96^{+0.16}_{-0.14}$
C7	6.44 ± 0.66	$0.92^{+0.27}_{-0.25}$	$0.55^{+0.02}_{-0.02}$	12.38/15	$0.70^{+0.38}_{-0.15}$	$1.46^{+0.26}_{-0.24}$
C_{combine}	7.68 ± 0.29	$0.67^{+0.09}_{-0.08}$	$0.73^{+0.01}_{-0.01}$	90.12/99	$0.95^{+0.07}_{-0.07}$	$1.20^{+0.08}_{-0.07}$
C8	>0.49					
C9	>0.97					
C10	>0.29					
C11	>0.23					
C12	>0.53					
XM1	>0.83					
XM2	8.18 ± 0.78	$0.20^{+0.07}_{-0.06}$	$0.94^{+0.30}_{-0.32}$	19.30/20	$0.82^{+0.04}_{-0.06}$	$0.50^{+0.06}_{-0.09}$
XM3	>0.55					

Notes: The N_H of one tbabs component was fixed to the line-of-sight value of $0.013 \times 10^{22} \text{ cm}^{-2}$, while the intrinsic N_H (second tbabs component) was left to free to vary. C_{combine} corresponds to combined observations C3–C7. Absorbed fluxes were calculated in the 0.5–8 keV energy range, while unabsorbed luminosities were derived assuming a distance of 7.6 Mpc. Quoted uncertainties correspond to the 90% confidence level for each parameter.

Table 3. Parameters of NGC 1097 ULX-3 from the tbabs*tbabs*(power-law+bbody) model, using the *XMM-Newton* MOS spectrum.

Parameters	Units	Values
N_H (a)	$10^{22} \times (\text{cm}^{-2})$	$0.09^{+0.03}_{-0.02}$
Γ		$1.42^{+0.33}_{-0.28}$
N_{norm}	$10^{-5} \times (\text{keV}^{-1} \text{ cm}^{-2} \text{ s}^{-1})$	$2.46^{+0.55}_{-0.48}$
kT	keV	$0.15^{+0.05}_{-0.04}$
N_{norm}	$10^{-6} \times (L_{39}/D_{10}^2)$	$1.3^{+0.90}_{-0.77}$
F_x (b)	$10^{-13} \times (\text{erg cm}^{-2} \text{ s}^{-1})$	$2.05^{+0.09}_{-0.07}$
L_x (c)	$10^{39} \times (\text{ergs s}^{-1})$	$10.60^{+2.90}_{-2.50}$
χ^2/dof		56.87/53

(a) Intrinsic hydrogen column density (N_H) obtained from the spectral fit, with the Galactic absorption fixed at $N_{H,\text{Gal}} = 0.013 \times 10^{22} \text{ cm}^{-2}$. (b) Absorbed flux in the 0.3–10 keV band. (c) Unabsorbed luminosity in the 0.3–10 keV band, assuming a distance of 16.8 Mpc. All uncertainties are quoted at the 90% confidence level.

point-like sources with *daofind* task, and their fluxes were measured with aperture photometry employing the DAOPHOT package (Stetson 1987) within IRAF² (Image Reduction and Analysis Facility). For the *JWST*/NIRCam observations, background estimation, source detection, and photometry were performed following the methodology of Allak (2023). Instrumental magnitudes were converted into Vega magnitudes using zero points (ZP) provided for WFC3/UVIS and ACS/WFC taken from Calamida et al. (2022), and the ZP calculator³. Sources

were required to exceed a 3σ significance above the local background. We then measured photometry using circular apertures of 3-pixel radius, with the background contribution subtracted using an annulus located nine pixels from the centroid.

Using the astrometric corrections reported by Guo et al. (2023), we identified three optical counterparts (X6a–Xc) for X-6 and two (X7a and X7b) for X-7 in the F606W and F814W bands. For NGC 1097 ULX-3, we searched the available catalogs (2MASS and Gaia DR3) for optical and NIR counterparts. Aside from the galaxy nucleus, we did not identify any reference sources with XRBs in these catalogs; therefore, the nucleus was used as the reference source for astrometric corrections. We corrected the relative astrometry between *Chandra* (CH7) and *HST* (F555W), *Chandra* and *JWST* (F115W), and *HST* and *JWST*, obtaining 95% confidence error radii of 0''.45, 0''.27, and 0''.10, respectively. Based on these results, we identified a unique optical and NIR counterpart within the astrometric error radius by applying a 3σ detection threshold over the background. Figure 7 shows the positions of the ULXs in Pan-STARRS RGB composite images (i, r, g bands), illustrating their distribution across the galaxy. In the NIRCam images (Figure 8), several faint NIR sources are present around the counterpart, but were not detected above the 1.5σ level. Therefore, we adopted the optical counterpart as the corresponding NIR counterpart of ULX-3. Figure 8 shows the positions of all three ULX counterparts. Tables 4 and 5 list the photometric results for the optical and NIR counterparts of NGC 4631 ULX X-6 and X-7, and NGC 1097 ULX-3.

Color–magnitude diagrams (CMDs) provide insights into the ages of the stellar populations surrounding ULXs, which may help constrain the nature of their donor stars. Isochrone models from the PAdova TRIeste Stellar Evolution Code (PARSEC) (Bressan et al. 2012) stellar evolution code are available for various telescope filters, including those of *HST*/ACS. We de-

² <https://iraf-community.github.io/>

³ <https://acszeropoints.stsci.edu/>

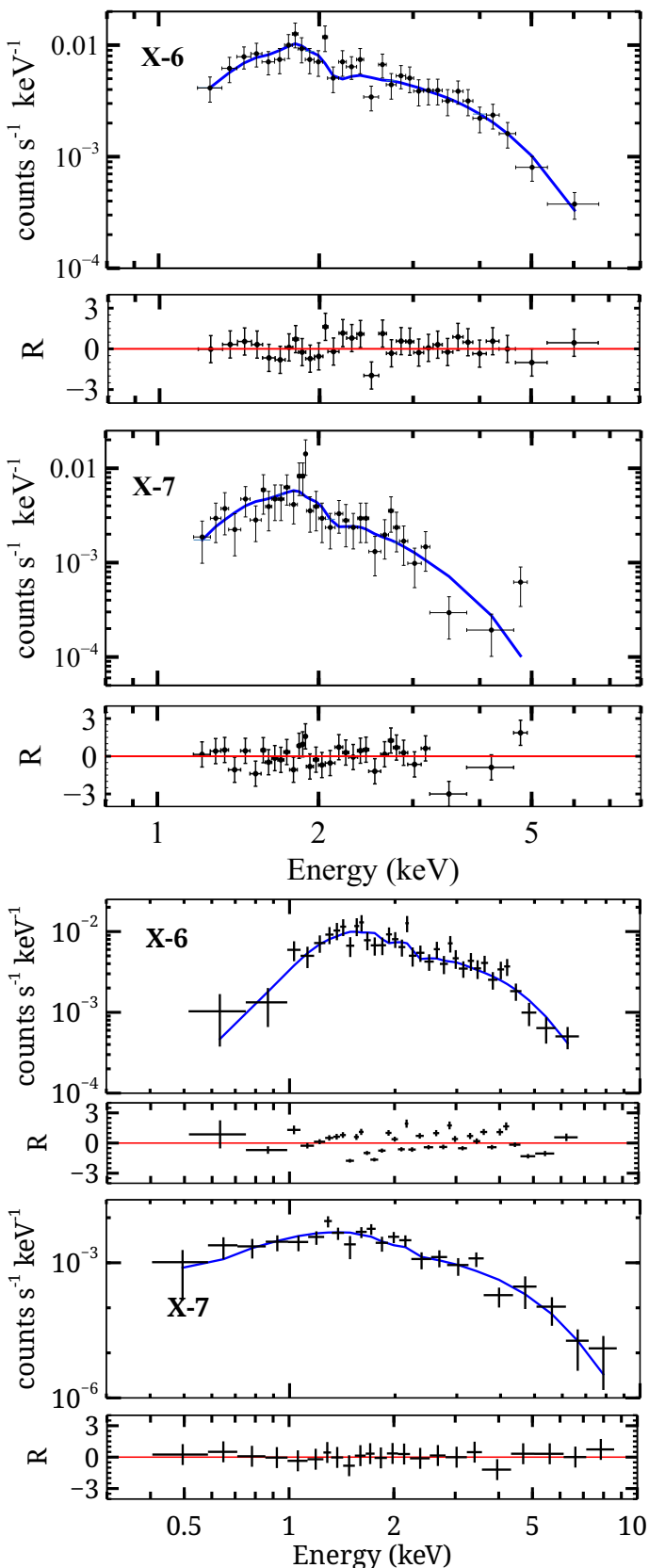


Fig. 2. *Chandra* energy spectra of NGC 4631 ULXs X-6 and X-7 (top two panels) and *XMM-Newton* (MOS) energy spectra (bottom two panels), with residuals shown as $R = (\text{data} - \text{model})/\text{error}$. In all panels, solid blue lines represent the diskbb model.

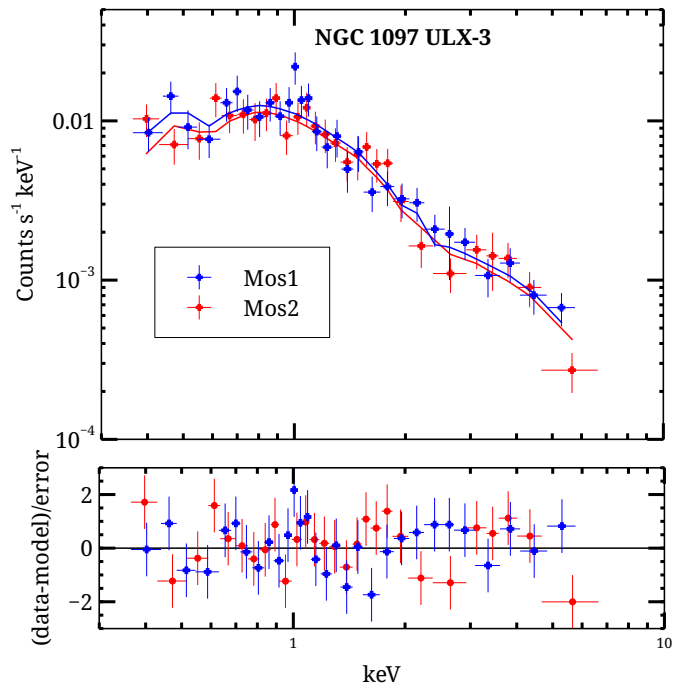


Fig. 3. Energy spectra for NGC 1097 ULX-3 obtained from *XMM-Newton* observations. Blue and red plus symbols represent MOS1 and MOS2 data, respectively. The power-law plus blackbody model fits are shown with green and red lines. All errors are at the 90% confidence level.

Table 4. Vega magnitudes of ULXs X-6 and X-7 optical counterparts in NGC 4631.

Source	Filter	Vega magnitude
X6a	F606W HST/WFC3	25.50 ± 0.06
X6a	F814W HST/WFC3	26.35 ± 0.08
X6b	F606W HST/WFC3	26.45 ± 0.08
X6b	F814W HST/WFC3	25.48 ± 0.08
X6c	F606W HST/WFC3	25.86 ± 0.04
X6c	F814W HST/WFC3	25.11 ± 0.10
X7a	F606W HST/WFC3	24.53 ± 0.04
X7a	F814W HST/WFC3	24.20 ± 0.06
X7b	F606W HST/WFC3	24.31 ± 0.04
X7b	F814W HST/WFC3	24.37 ± 0.06

derived the upper limit extinction, A_V , using the method of Guo et al. (2023) and used this value to correct the isochrones. Using the average N_H values from Tables 1 and 2, we derived $E(F606W-F814W)$ values of 2.90 mag and 1.72 mag for X-6 and X-7, respectively. Figure 9 shows the CMDs for X-6 and X-7, plotted as F606W versus F606W-F814W, with isochrones and field sources located within 2'' radius circles centered on the ULX positions, alongside the optical counterparts. For ULX-3, we only constructed an NIR CMD due to the limited optical data. The *HST*/F814W photometry shows variability likely originating from the accretion disk; nonsimultaneous filters prevent reliable color measurements. The source is extremely faint in the UVIS bands and F438W detection is consistent with an upper limit, making an optical CMD infeasible. In contrast, the *JWST*/NIRCam data show no variability; therefore, we were able to construct a single-epoch NIR CMD. The NIR CMD was constructed using F115W and F277W photometry, adopting a distance of 16.8 Mpc and an upper limit extinction of 0.06 mag (Figure 10).

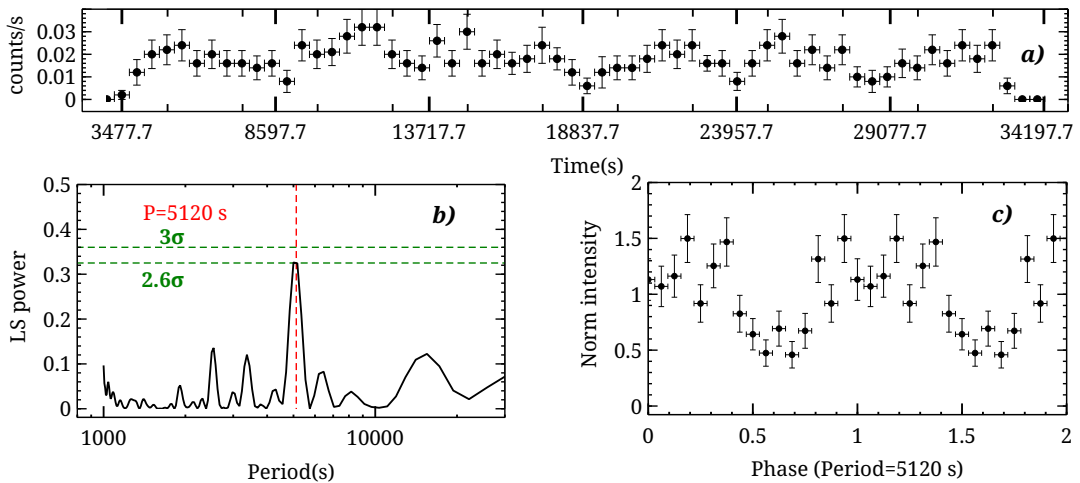


Fig. 4. Timing analysis of NGC 4631 ULX X-6 from the C2 observation. (a) Background-subtracted light curve in the 0.3–10 keV band with a bin size of 500 s. (b) Lomb–Scargle periodogram showing a peak at $P = 5120$ s (~ 1.42 h) at the 2.6σ confidence level. (c) Folded light curve at $P = 5120$ over two cycles, normalized to the mean count rate.

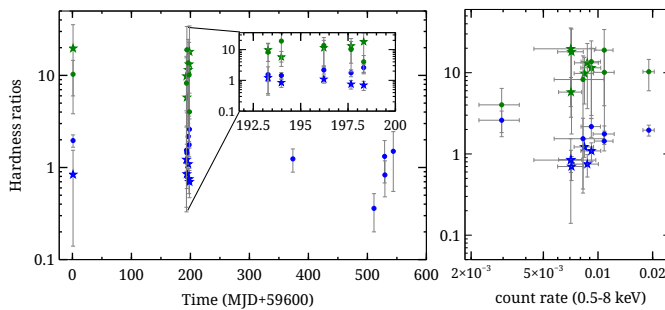


Fig. 5. Left panel: Hardness ratios versus time. Right panel: Hardness–intensity diagram of ULXs X-6 and X-7. X-6 and X-7 are represented by filled circles and stars, respectively. Green and blue colors show the medium/soft and hard/medium ratios, respectively. All error bars represent the 1σ level.

Table 5. Vega magnitudes of optical and infrared counterparts of ULX-3.

Filter	Instrument	Date	Vega magnitude
F275W	HST/WFC3	2020-08-14	26.29 ± 0.47
F336W	HST/WFC3	2014-02-20	26.55 ± 0.38
F438W	HST/WFC3	2014-02-20	>27.60
F555W	HST/WFC3	2020-08-14	>27.40
F814W	HST/ACS/WFC	2004-06-05	>26.50
F814W	HST/WFC3	2014-02-20	>26.00
F814W	HST/ACS/WFC	2019-05-28	25.74 ± 0.26
F115W	JWST/NIRCam	2023-12-27	22.97 ± 0.08
F115W	JWST/NIRCam	2024-09-29	22.55 ± 0.04
F200W	JWST/NIRCam	2024-09-29	22.40 ± 0.04
F277W	JWST/NIRCam	2024-09-29	22.25 ± 0.09
F300M	JWST/NIRCam	2023-12-27	22.25 ± 0.11
F335M	JWST/NIRCam	2023-12-27	22.25 ± 0.09
F335M	JWST/NIRCam	2024-09-29	22.45 ± 0.08
F360M	JWST/NIRCam	2024-09-29	22.40 ± 0.08
F444W	JWST/NIRCam	2024-09-29	22.75 ± 0.09

For ULX-3, we converted the observed magnitudes into fluxes using the corresponding zeropoints and adopted the pivot wavelength of each *JWST*/NIRCam filter. The resulting SED is

well fit by a blackbody model with a best-fit temperature of $T = 3300 \pm 140$ K and a reduced chi-square of $\chi^2/\text{dof} = 0.95$ for four degrees of freedom (Figure 11).

4. Results and discussion

4.1. NGC 4631 X-6 and X-7

4.1.1. Spectral modeling and variability

In NGC 4631, we identified two new transient ULX candidates, X-6 and X-7, from observations conducted between 2021 and 2023. Across 13 *Chandra* observations (C1–C13) and three *XMM-Newton* observations (XM1–XM3), we did not detect X-6 in C1, XM1, or XM3. We detected X-7 source only in XM2 and in five *Chandra* observations (C2–C7). We also examined *Swift*/XRT PC observations using the *Swift-XRT* data products tool⁴ to investigate the visibility of X-6 and X-7.

For X-6, both the power-law and diskbb models yield N_{H} values that vary by nearly an order of magnitude in *Chandra* observations when intrinsic absorption is left free. The N_{H} variability may reflect genuine changes in the local environment, but could also result from statistical uncertainties or spectral modeling limitations. We therefore fixed N_{H} to its average value and repeated the spectral fits (Table 1). After applying this procedure, we obtained notable improvements in the reduced χ^2 values for both the diskbb and power-law models. Applying simple phenomenological models to the X-6 spectra, we found that the two models could not be distinguished in the *Chandra* datasets, likely because of limited data quality. The power-law photon index (Γ) ranges between 1.6 and 2.8. For Galactic BH binaries (BHBs), $\Gamma \sim 1.4$ –2.4 typically corresponds to the hard state, characterized by Comptonization of disk photons in a hot, optically thin corona (e.g., Remillard & McClintock 2006; Done et al. 2007). For X-6, Γ remains <2.4 in nearly all *Chandra* observations (except C8), indicating that the source resides predominantly in the hard state. Based on the power-law model, X-6 exhibits $L_{\text{X}} = (1–4) \times 10^{39}$ erg s^{−1} in the 0.5–8 keV band.

Furthermore, X-6 is well described by the diskbb model, with the inner disk temperature (T_{in}) varying between 0.8 and 2

⁴ https://www.swift.ac.uk/user_objects/

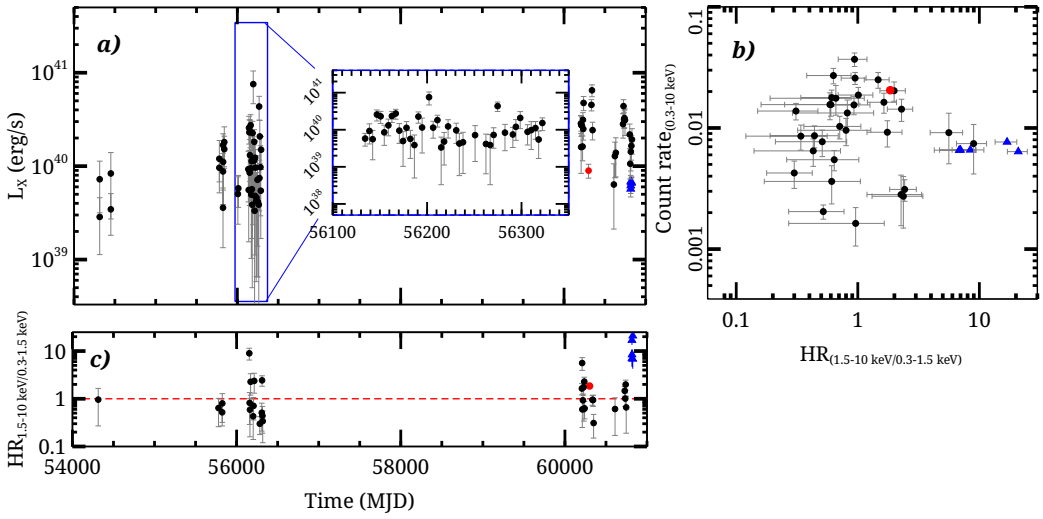


Fig. 6. Long-term X-ray properties of ULX-3. (a) L_X light curve in the 0.3–10 keV band, with the inset showing a zoomed-in view for clarity (MJD 56134–56322). (b) Hardness–intensity diagram, where the count rate in the 0.3–10 keV band is plotted against the hardness ratio $HR_{1.5-10\text{ keV}/0.3-1.5\text{ keV}}$. (c) Temporal evolution of the hardness ratio $HR_{1.5-10\text{ keV}/2-3.5\text{ keV}}$ as a function of time (MJD), with the dashed red line marking the reference level. *Swift/XRT*, *XMM-Newton*, and *Chandra* observations are shown with filled black and red circles and blue triangles, respectively.

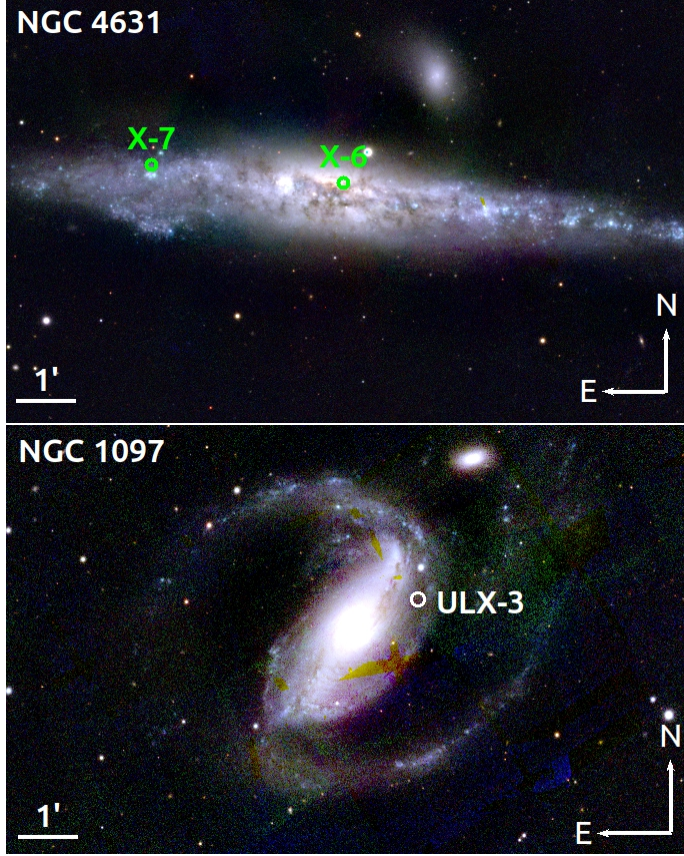


Fig. 7. Visualization of new ULXs in NGC 4631 (left) and NGC 1097 (right), on Pan-STARRS RGB (i, r, g) composite images. The positions of the ULXs are indicated with green and white circles.

keV. Using the diskbb spectral model, X-6 exhibits $L_X = (0.6 - 2.7) \times 10^{39}$ erg s⁻¹ in the 0.5–8 keV band. For X-7, among all the single and multi-component models tested in XSPEC, only the diskbb model provides acceptable fits, yielding inner disk tem-

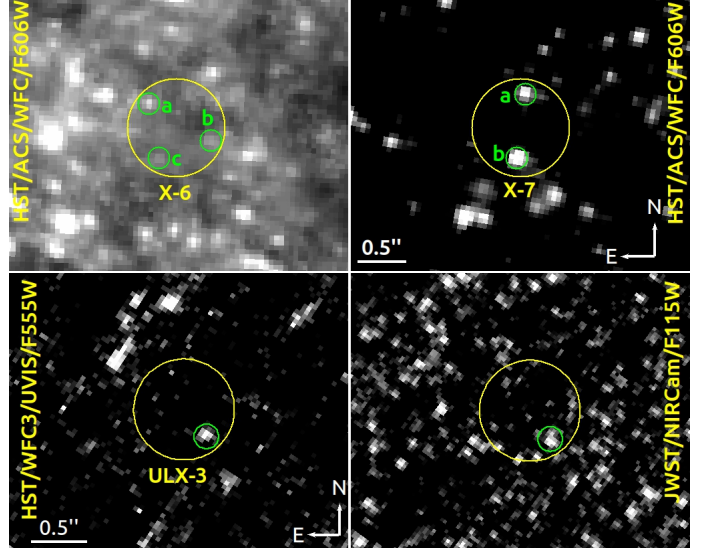


Fig. 8. Upper panels: Optical counterparts of ULXs X-6 and X-7 in NGC 4631 (upper panels). The solid yellow circles have a radius of 0.5''. The small green circles represent the candidate counterparts. Bottom panels: Position of the optical counterpart (green circle) of ULX-3 on *HST* (left) and *JWST* (right) images. The solid yellow circles show the astrometric error radius of 0.45''

peratures of $kT_{\text{in}} \sim 0.6 - 1$ keV for roughly half of the dataset. For the C2–C7 observations, X-7 exhibits $L_X = (1 - 2) \times 10^{39}$ erg s⁻¹ in the 0.5–8 keV band, based on the diskbb spectral model. The temperatures indicate that X-ray emission is dominated by accretion disk processes, consistent with Galactic XRBs in the thermal state at high accretion rates. Such disk-dominated spectral behavior has been reported in several ULX studies, with thermal components consistent with super-Eddington accretion or slim disk models (e.g., Gladstone et al. 2009; Luangtip et al. 2016). To search for spectral state transitions, we constructed hardness ratios as a function of time and hardness–intensity di-

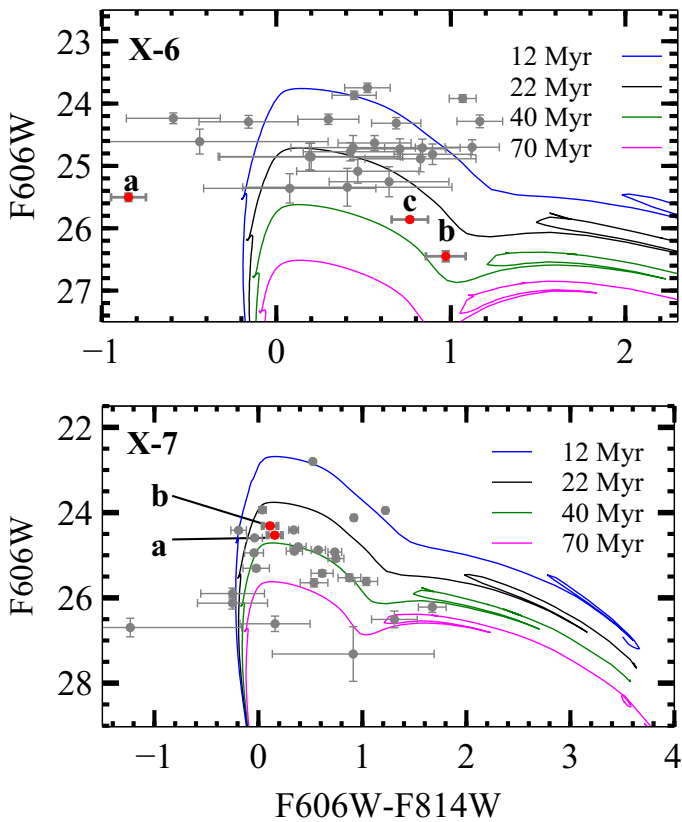


Fig. 9. Color-magnitude diagrams of NGC 4631 X-6 and X-7. The filled red and gray circles represent candidate counterparts and field stars, respectively.

ograms (Figure 5). Source X-6 predominantly occupies the hard state, with episodes indicating transitions from hard to intermediate and back to hard, whereas source X-7 resides mostly in the intermediate state.

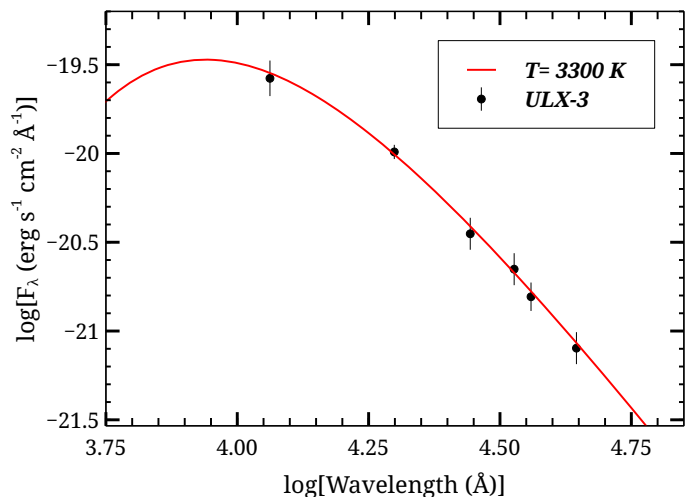


Fig. 11. Near-IR SED of NGC 1097 ULX-3. The solid red line represents a blackbody model with a temperature of 3300 K. The SED is constructed from simultaneous NIRCam observations.

The X-6 and X-7 ULXs do not show significant variability on short timescales of a few days. We detected a ~ 5120 s, low-amplitude, low-significance (2.6σ) periodic modulation for NGC 4631 X-6 only in the C2 observation. Hour-scale (4–7 ks) quasi-periodic behavior has been reported in some ULXs (e.g., the M74 ULX; Liu et al. 2005), showing that this timescale is physically plausible for accretion-flow variability. In contrast, orbital periods in ULXs are typically days, except for a few systems with Wolf-Rayet donors (e.g., Lin et al. 2023), which show hour-scale periods. Because the period falls below conventional significance thresholds, deeper and higher signal-to-noise observations are needed to constrain the origin of this periodic feature.

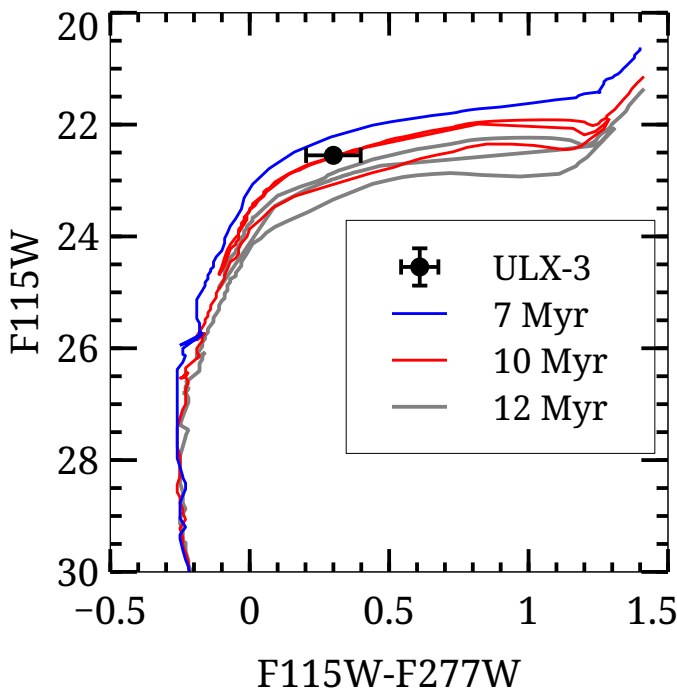


Fig. 10. Color-magnitude diagram of NGC 1097 ULX-3.

4.1.2. $L_X - T_{\text{in}}$ relation

We investigated the relationship between disk luminosity (L_{disc}) and the color temperature of the accretion disk (T_{in}) for X-6 and X-7. In Galactic BHBs, the X-ray emission in the thermal dominant state is generally produced by a geometrically thin, optically thick disk, which is well described by the standard accretion disk model (Shakura & Sunyaev 1973). Within this framework, L_{disc} and T_{in} are expected to follow the relation $L_{\text{disc}} \propto T_{\text{in}}^4$ if the inner disk radius remains constant. Testing this correlation probes accretion geometry and physical conditions, while deviations from the expected trend can reveal structural changes in the disk, such as truncation, strong Comptonization, or transitions away from the thin-disk regime, particularly at high luminosities (Kubota & Done 2004; Done et al. 2007). Figure 12 shows the relationship between L_X and T_{in} for X-6 using diskbb spectral parameters (Tables 1 and 2). The data reveal a strong positive correlation of the form $L_X \propto T^{\alpha}$, with a best-fit slope $\alpha = 3.68 \pm 0.41$ (dashed line), consistent within the uncertainties with the canonical $L \propto T^4$ relation predicted by the standard accretion disk model (Shakura & Sunyaev 1973). This relation suggests that X-6 is likely in a disk-dominated accretion regime with a relatively stable inner disk radius. The outlier, denoted C5, significantly deviates from the observed trend, lying at a higher temperature but lower luminosity than expected. This may indicate a temporary transition to a different spectral state, obscuration, or a change in viewing geometry. For example, Feng & Kaaret (2007)

found that NGC 1313 X-2 exhibited a relation consistent with $L \propto T^4$ during certain states, indicating a constant inner disk radius. Transient ULXs, such as XMMU J004243.6+412519 in M31, have also shown L-T tracks broadly consistent with the expected T^4 relation. (Middleton et al. 2013). Overall, the $L_X - T_{in}$ trend observed in X-6 supports a stellar-mass compact object accreting in a high state, rather than an intermediate-mass BH scenario, which typically exhibits cooler disks at high luminosities (Merloni et al. 2003).

In addition, the diskbb normalization parameter provides an estimate of the apparent inner disk radius: $N = \left(\frac{R_{in}/\text{km}}{D_{10}}\right)^2 \cos \theta$, where N is the normalization, $R_{in,obs}$ is the observed inner disk radius in km, and D_{10} is the distance to the source in units of 10 kpc. Using $N_{min} = 1.6 \times 10^{-3}$ and $N_{max} = 25 \times 10^{-3}$, the observed inner disk radii are 28 and 110 km. To account for spectral hardening and boundary condition effects, we applied a correction factor of $\kappa^2 \xi = 1.19$ (Shimura & Takahara 1995; Kubota et al. 1998). Therefore, the corrected values of $R_{in,min}$ and $R_{in,max}$ are 30 and 130 km, respectively. Assuming that the inner disk radius corresponds to the innermost stable circular orbit (ISCO) of a Schwarzschild BH, $R_{in} \approx R_{ISCO} = 6GM/c^2$, the mass is $\frac{M}{M_\odot} = \frac{R_{in}}{8.86 \text{ km}}$. The estimated mass range is $\sim 5-15 M_\odot$, increasing to $\sim 5-20 M_\odot$ for an assumed disk inclination of 60° . These values are consistent with a stellar-mass BH.

We calculated the accretion rate to assess the accretion regime of ULXs following the method described in Section 4.4 of Ghosh & Rana (2023). For X-6, we estimate an accretion rate of $\dot{m}_0 \sim 4-9$, depending on the assumed compact object mass in the range $5-15 M_\odot$. This estimate places the source in a moderately super-Eddington regime, where the spherization radius ($R_{sph} = 270-850$ km) lies significantly beyond the inner disk radius, $R_{in} = 30-130$ km. This structure between R_{sph} and R_{in} is consistent with the expectation that radiation pressure drives strong outflows at larger radii, while the inner accretion disk remains relatively compact. The derived beaming factors ($b \sim 0.9-2.3$) further suggest that the observed L_X of X-6 does not require strong geometric collimation, supporting a scenario in which the source is powered by nearly isotropic emission from a stellar-mass BH in a super-Eddington state (Ghosh & Rana 2023). For the transient ULX X-7, the L_X versus T_{in} relation yields a slope of $\alpha = 2.54 \pm 0.55$, which is lower than the $\alpha = 4$ ($L \propto T^4$) scaling expected for a standard thin disk. However, according to the α range ($0 < \alpha < 4$) defined by Majumder et al. (2025), X-7 lies within the regime corresponding to slim-disk behavior (Watarai et al. 2000; Kubota & Makishima 2004). Similarly, Brightman et al. (2016) report that broadband spectral analyses of ULXs support the presence of optically thick, geometrically slim accretion disks, consistent with the observed parameters of X-7.

4.1.3. Optical counterparts of ULXs X-6 and X-7

The optical counterparts of ULXs X-6 and X-7 appear faint in both filters, consistent with the typical magnitudes observed for ULX optical counterparts. Because multiple possible counterparts are detected for both sources, we cannot place reliable constraints on their optical emission. Nevertheless, the CMDs allow us to derive some constraints on their ages and masses. However, all three candidate counterparts of X-6 occupy positions on the CMD that are clearly distinct from the field stars in the surrounding region (Figure 9), suggesting that they may belong to a different stellar population or have followed a different evolutionary path. The source X6a, which is relatively brighter than the

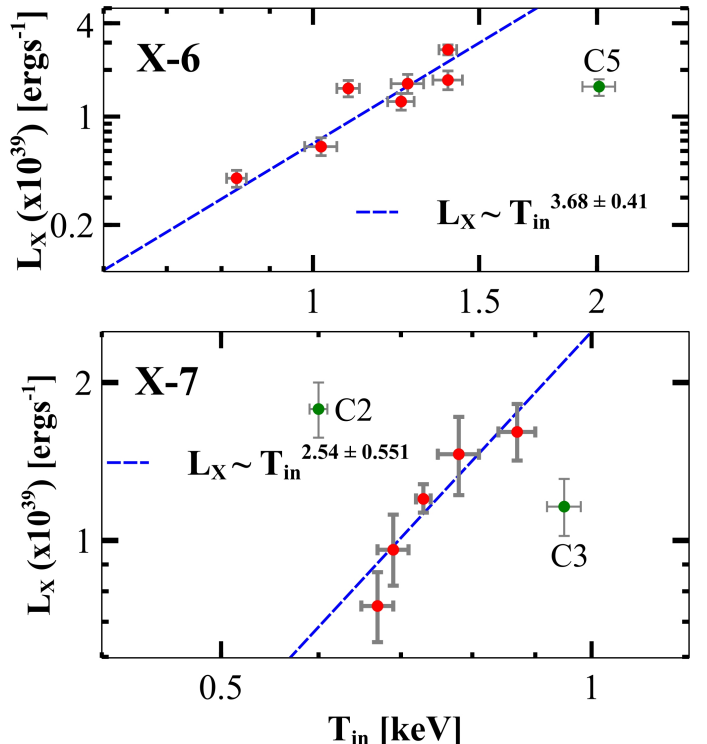


Fig. 12. Luminosity (L_X) versus inner disk temperature (T_{in}) diagrams of X-6 (top) and X-7 (bottom) inferred from the diskbb model. The data points use T_{in}^* and L_X^* and T_{in} and L_X values from Tables 1 and 2.

other counterparts, is distinct from the isochrones on the CMD. The exceptionally blue color of X6a may be affected by observational limitations. Although we applied identical photometric procedures to all sources, the *HST* data are limited and nonsimultaneous, leaving the optical variability of X6a unknown. If X6a is the true counterpart, its optical emission may be dominated by the accretion disk rather than by the donor star, which would produce a displaced position in the CMD. Deeper and simultaneous optical and X-ray observations are required to establish the true properties of X6a.

Based on the CMDs, X-6b, X-6c, X-7a, and X-7b have estimated ages of 30–40 Myr and masses in the range $7-9 M_\odot$, consistent with an HMXB classification. Because continuous optical monitoring and simultaneous optical and X-ray observations are unavailable, the variability of these candidate counterparts remains uncertain. Consequently, we could not derive the F_X/F_{optic} ratio for X-6 and X-7, which serves to constrain the nature of the sources through their X-ray-to-optical flux comparison (Maccacaro et al. 1988; Stocke et al. 1991).

4.2. NGC 1097 ULX-3

In this study, we analyzed NGC 1097 ULX-3 in detail for the first time and identify it as an ULX based on its X-ray spectral and temporal properties, with additional observations in the optical and infrared bands. We detected ULX-3 in the five most recent *Chandra* observations between 21 May and 31 May 2025, with a stable $L_X \sim (6-7) \times 10^{39} \text{ erg s}^{-1}$ and no significant variability on short timescales. The *XMM-Newton* observation performed in 2023 shows a comparable luminosity level of $L_X \sim 10^{40} \text{ erg s}^{-1}$. Long-term monitoring with *Swift/XRT* between 2 August 2007 and 6 June 2025 reveals significant variability. During this 18-year period, L_X of ULX-3 varied between 3×10^{39} and 8×10^{40}

erg s⁻¹. Such long-term flux variation suggests that ULX-3 is a highly variable source, likely driven by significant changes in the accretion rate, accretion state transitions, or geometric effects such as variable absorption or accretion-disk precession. Overall, these results suggest that ULX-3 remains relatively stable on short timescales, as indicated by the recent *Chandra* and *XMM-Newton* observations, but exhibits obvious variability over long timescales spanning years to decades, as revealed by the *Swift*/XRT monitoring.

The X-ray spectrum of ULX-3 is best described by a two-component model consisting of a soft thermal blackbody and a hard power-law component (power-law plus bbody). The soft thermal component, with a temperature of $kT \approx 0.15$ keV, is consistent with the soft excess observed in many ULXs (Gladstone et al. 2009; Sutton et al. 2013) and is typically attributed to emission from an optically thick wind or outflow launched from a supercritical accretion disk (Poutanen et al. 2007; Middleton et al. 2015). This component may correspond to the wind photosphere or to the outer, geometrically thick regions of the accretion flow. Such hard spectral slopes are commonly associated with the so-called HUL state in ULXs (Gladstone et al. 2009; Sutton et al. 2013; Heida et al. 2014), in which the inner regions of the accretion flow may be partially visible through the wind funnel, allowing Comptonized emission from a hot corona or the innermost disk to dominate at higher energies. The combination of a low-temperature thermal component and a hard power-law tail supports a super-Eddington accretion scenario for ULX-3, likely involving a stellar-mass compact object surrounded by a geometrically and optically thick accretion structure (Pinto et al. 2021).

To investigate spectral state transitions, we constructed hardness evolution and hardness intensity diagrams (Figure 6, panels b and c). At high count rates, the source spectrum becomes softer, consistent with a thermal disk-dominated (high-soft) state, whereas at low count rates, the spectrum hardens, indicative of a corona- or Comptonization-dominated (low-hard) state. Such a correlation is a signature of accretion-powered variability, linking luminosity changes to transitions between spectral states. In Galactic XRBs, such transitions are well characterized and often correspond to changes between low-hard and high-soft states driven by variations in the mass accretion rate (Remillard & McClintock 2006; Done et al. 2007). In ULXs, however, spectral state transitions are more complex due to their potential super-Eddington luminosities and geometric beaming effects (King 2009). The observed transitions in this source may reflect different accretion modes onto a compact object, which could be either a stellar-mass BH or an NS (Poutanen et al. 2007; Bachetti et al. 2014; Middleton et al. 2015; Walton et al. 2018). Optically thick, radiatively driven outflows could obscure the inner hot regions of the disk, leading to softer spectra when observed at moderate inclination angles. In the case of harder spectra at even higher flux levels, changes in wind geometry, collimation, or the reemergence of the innermost accretion flow could indicate a transition in the accretion regime (Kawashima et al. 2012). Overall, the spectral state transitions observed in NGC 1097 ULX-3 reinforce the emerging picture that ULXs form a heterogeneous population, displaying diverse accretion behaviors that span the regime between Galactic XRBs and super-Eddington accretion, implying that ULX-3 could be powered either by a stellar-mass BH or an NS.

We identified a unique optical and NIR counterpart within the astrometric error radius of ULX-3. The optical counterpart is fainter than typical ULX counterparts, with $F555W \simeq m_V = 27.40$ mag ($M_V \simeq -4$ mag). In the F814W filter, the variability of

the source is quantified as the difference between the faintest and brightest magnitudes measured over three epochs (2004–2019), yielding $\Delta m_{F814W} \simeq 0.8$ mag and suggesting intrinsic variability in the optical emission of ULX-3. The variable X-ray emission is likely linked to the observed optical variability, suggesting that accretion processes dominate the optical emission.

In contrast, the NIR observations obtained between 27 December 2023 and 29 September 2024 reveal that the source remains nearly constant in magnitude. Furthermore, we can exclude a variable jet contribution to the NIR emission, since the infrared emission remains constant. Using simultaneous *JWST*/NIRCam filters, we constructed the spectral energy distribution (SED) of the ULX counterpart and fit it with a blackbody model with a temperature of ~ 3300 K (see Figure 11). The effective temperature derived is too high to be attributed to circumbinary material or dust (Dudik et al. 2016; Lau et al. 2017, 2019; Allak 2023) and instead falls within the expected range for RSGs. Adopting a blackbody temperature of 3300 K, we used the relation $F_\lambda = \pi B_\lambda(T) (R/D)^2$, together with NIRCam photometry at a distance of 16.8 Mpc, to derive an RSG radius of $\sim 200 R_\odot$. The absolute magnitude of the counterpart is $M_{277} = -8.9$ mag. In the NIR CMD, this value lies on the evolutionary tracks of ~ 15 –20 M_\odot stars with ages of 7–12 Myr, indicating that its CMD position is consistent with the RSG evolutionary branch.

5. Conclusions

In this work, we report the identification and characterization of three new ULXs in NGC 4631 and NGC 1097. Our main findings can be summarized as follows.

NGC 4631 X-6 exhibits L_X variability of about an order of magnitude and recurrent spectral variability. Spectral analyses support its classification as a stellar-mass BH candidate accreting in a super-Eddington regime. The L_X – T_{in} relation follows the $L \propto T^4$ trend expected for a standard thin disk, supporting the interpretation of X-6 as a stellar-mass BH accretor.

NGC 4631 X-7, a transient ULX, displays long-term L_X variability and disk-dominated spectra with inner disk temperatures of 0.5–1 keV. Its photometric properties are consistent with a donor star of 7 – $9 M_\odot$ and an age of 30–40 Myr, supporting an HMXB scenario. Moreover, the $L \propto T^4$ trend expected for standard thin disks provides evidence for a slim disk accretion state. Finally, our analysis indicates that both X-6 and X-7 have properties consistent with normal HMXBs hosting BHs with masses of $\sim 20 M_\odot$.

NGC 1097 ULX-3 exhibits strong long-term variability, with L_X changes up to a factor of ~ 30 . Spectral state transitions indicate that ULX-3 is a stellar-mass BH or NS accretor in a super-Eddington state. We identify a unique optical and NIR counterpart to ULX-3. Although the optical emission is highly variable, the NIR counterpart remains nearly constant. For the optical counterpart of ULX-3, the NIR SED is consistent with a blackbody temperature of ~ 3300 K and a stellar radius of $\sim 200 R_\odot$, providing strong evidence that the source is an RSG donor star.

For the three ULXs in the two host galaxies, additional multi-wavelength observations will be crucial to constrain their environments, donor stars, and accretion processes, ultimately leading to a clearer understanding of their nature.

Acknowledgements. This work is partially supported by the Bundesministerium für Wirtschaft und Energie through the Deutsches Zentrum für Luft- und Raumfahrt e.V. (DLR) under the grant 50 OR 2517. LD acknowledges funding from the Deutsche Forschungsgemeinschaft (DFG, German Research Foundation) –

Projektnummer 549824807. AA and YA acknowledge support provided by the TÜBİTAK through project number 124F004. We thank the referee for her/his careful reading of the manuscript and for the valuable comments, which helped us to improve the paper.

References

Allak, S. 2022, MNRAS, 517, 3495
 Allak, S. 2023, MNRAS, 526, 5765
 Allak, S. & Akyuz, A. 2025, A&A, 694, A301
 Allak, S., Akyuz, A., Sonbas, E., & Dhuga, K. S. 2022, MNRAS, 515, 3632
 Arnaud, K. A. 1996, in Astronomical Society of the Pacific Conference Series, Vol. 101, Astronomical Data Analysis Software and Systems V, ed. G. H. Jacoby & J. Barnes, 17
 Bachetti, M., Harrison, F. A., Walton, D. J., et al. 2014, Nature, 514, 202
 Bressan, A., Marigo, P., Girardi, L., et al. 2012, MNRAS, 427, 127
 Brightman, M., Bachetti, M., Earnshaw, H. P., et al. 2019, BAAS, 51, 352
 Brightman, M., Hameury, J.-M., Lasota, J.-P., et al. 2023, ApJ, 951, 51
 Brightman, M., Harrison, F., Walton, D. J., et al. 2016, ApJ, 816, 60
 Calamida, A., Bajaj, V., Mack, J., et al. 2022, AJ, 164, 32
 Carpano, S., Haberl, F., Maitra, C., & Vasilopoulos, G. 2018, MNRAS, 476, L45
 Carpano, S., Pollock, A. M. T., King, A. R., Wilms, J., & Ehle, M. 2007, A&A, 471, L55
 Dickey, J. M. & Lockman, F. J. 1990, ARA&A, 28, 215
 Done, C., Gierliński, M., & Kubota, A. 2007, A&A Rev., 15, 1
 Ducci, L., Mereghetti, S., Pintore, F., et al. 2025, arXiv e-prints, arXiv:2511.04282
 Dudik, R. P., Berghea, C. T., Roberts, T. P., et al. 2016, ApJ, 831, 88
 Earnshaw, H. P., Heida, M., Brightman, M., et al. 2020, ApJ, 891, 153
 Fabrika, S., Ueda, Y., Vinokurov, A., Sholukhova, O., & Shidatsu, M. 2015, Nature Physics, 11, 551
 Fabrika, S. N., Atapin, K. E., Vinokurov, A. S., & Sholukhova, O. N. 2021, Astrophysical Bulletin, 76, 6
 Feng, H. & Kaaret, P. 2007, ApJ, 660, L113
 Fruscione, A., McDowell, J. C., Allen, G. E., et al. 2006, in Society of Photo-Optical Instrumentation Engineers (SPIE) Conference Series, Vol. 6270, Observatory Operations: Strategies, Processes, and Systems, ed. D. R. Silva & R. E. Doxsey, 62701V
 Ghosh, T. & Rana, V. 2023, ApJ, 949, 78
 Gladstone, J. C., Copperwheat, C., Heinke, C. O., et al. 2013, ApJS, 206, 14
 Gladstone, J. C., Roberts, T. P., & Done, C. 2009, MNRAS, 397, 1836
 Greene, J. 2022, in 44th COSPAR Scientific Assembly. Held 16-24 July, Vol. 44, 2201
 Guo, J., Wu, J., Feng, H., et al. 2023, ApJ, 946, 72
 Gúrpide, A., Godet, O., Koliopanos, F., Webb, N., & Olive, J.-F. 2021a, A&A, 649, A104
 Gúrpide, A., Godet, O., Vasilopoulos, G., Webb, N. A., & Olive, J. F. 2021b, A&A, 654, A10
 Heida, M., Jonker, P. G., Torres, M. A. P., et al. 2014, MNRAS, 442, 1054
 Heida, M., Jonker, P. G., Torres, M. A. P., et al. 2016, MNRAS, 459, 771
 Heinzel, D., Duschl, W. J., Mineshige, S., & Ohsuga, K. 2006, arXiv preprint astro-ph/0610544
 Israel, G. L., Belfiore, A., Stella, L., et al. 2017, Science, 355, 817
 Kaaret, P., Feng, H., & Roberts, T. P. 2017, ARA&A, 55, 303
 Kajava, J. J. E. & Poutanen, J. 2009, MNRAS, 398, 1450
 Kawashima, T., Ohsuga, K., Mineshige, S., et al. 2012, ApJ, 752, 18
 King, A., Lasota, J.-P., & Middleton, M. 2023, New A Rev., 96, 101672
 King, A. R. 2009, MNRAS, 393, L41
 Kubota, A. & Done, C. 2004, MNRAS, 353, 980
 Kubota, A. & Makishima, K. 2004, ApJ, 601, 428
 Kubota, A., Tanaka, Y., Makishima, K., et al. 1998, PASJ, 50, 667
 Lau, R. M., Heida, M., Kasliwal, M. M., & Walton, D. J. 2017, ApJ, 838, L17
 Lau, R. M., Heida, M., Walton, D. J., et al. 2019, ApJ, 878, 71
 Lin, Z., Soria, R., & Swartz, D. A. 2023, ApJ, 954, 46
 Liu, J. 2011, ApJS, 192, 10
 Liu, J., Bregman, J. N., & McClintock, J. E. 2009, ApJ, 690, L39
 Liu, J.-F., Bregman, J. N., Lloyd-Davies, E., et al. 2005, ApJ, 621, L17
 Luangtip, W., Roberts, T. P., & Done, C. 2016, MNRAS, 460, 4417
 Maccacaro, T., Gioia, I. M., Wolter, A., Zamorani, G., & Stocke, J. T. 1988, ApJ, 326, 680
 Majumder, S., Das, S., & Nandi, A. 2025, MNRAS, 539, 2064
 Merloni, A., Heinz, S., & di Matteo, T. 2003, MNRAS, 345, 1057
 Middleton, M. J., Miller-Jones, J. C. A., Markoff, S., et al. 2013, Nature, 493, 187
 Middleton, M. J., Walton, D. J., Fabian, A., et al. 2015, MNRAS, 454, 3134
 Mondal, S., Różańska, A., Bagińska, P., Markowitz, A., & De Marco, B. 2021, A&A, 651, A54
 Motch, C., Pakull, M. W., Soria, R., Grisé, F., & Pietrzyński, G. 2014, Nature, 514, 198
 Mushtukov, A. A., Suleimanov, V. F., Tsygankov, S. S., & Ingram, A. 2017, MNRAS, 467, 1202
 Nemmen, R. S., Storchi-Bergmann, T., Yuan, F., et al. 2006, ApJ, 643, 652
 Pinto, C., Mehdipour, M., Walton, D. J., et al. 2020, MNRAS, 491, 5702
 Pinto, C., Soria, R., Walton, D. J., et al. 2021, MNRAS, 505, 5058
 Pinto, C., & Walton, D. J. 2023, arXiv e-prints, arXiv:2302.00006
 Poutanen, J., Lipunova, G., Fabrika, S., Butkevich, A. G., & Abolmasov, P. 2007, MNRAS, 377, 1187
 Remillard, R. A. & McClintock, J. E. 2006, ARA&A, 44, 49
 Robba, A., Pinto, C., Pintore, F., et al. 2022, MNRAS, 515, 4669
 Roberts, T. P., Walton, D. J., Mackenzie, A. D. A., Heida, M., & Scaringi, S. 2023, MNRAS, 525, 3330
 Shakura, N. I. & Sunyaev, R. A. 1973, A&A, 24, 337
 Shimura, T. & Takahara, F. 1995, ApJ, 445, 780
 Soria, R. & Ghosh, K. K. 2009, ApJ, 696, 287
 Soria, R., Hakala, P. J., Hau, G. K. T., Gladstone, J. C., & Kong, A. K. H. 2012, MNRAS, 420, 3599
 Stetson, P. B. 1987, PASP, 99, 191
 Stocke, J. T., Morris, S. L., Gioia, I. M., et al. 1991, ApJS, 76, 813
 Sutton, A. D., Roberts, T. P., Gladstone, J. C., et al. 2013, MNRAS, 434, 1702
 Tao, L., Feng, H., Grisé, F., & Kaaret, P. 2011, ApJ, 737, 81
 van Haften, L. M., Maccarone, T. J., Rhode, K. L., Kundu, A., & Zepf, S. E. 2019, MNRAS, 483, 3566
 Vinokurov, A., Fabrika, S., & Atapin, K. 2018, ApJ, 854, 176
 Walton, D. J., Fürst, F., Heida, M., et al. 2018, ApJ, 856, 128
 Walton, D. J., Heida, M., Bachetti, M., et al. 2021, MNRAS, 501, 1002
 Watarai, K.-y., Fukue, J., Takeuchi, M., & Mineshige, S. 2000, PASJ, 52, 133

Appendix A: X-ray, optical, and NIR observations of the ULXs

Table A.1. Log of NGC 4631 and NGC 1097 observations.

Label	Filter	ObsID	Instrument	Exp. (ks)	Date
NGC 4631					
C1	797		ACIS-S	59.21	2000-04-16
XM1	0110900201		EPIC	54.8	2002-06-28
XM2	0890710101		EPIC	33.0	2021-12-28
C2	25777		ACIS-S	29.03	2022-01-22
C3	25220		ACIS-S	22.77	2022-08-02
C4	26484		ACIS-S	18.82	2022-08-02
C5	26485		ACIS-S	20.80	2022-08-05
C6	26486		ACIS-S	14.88	2022-08-06
C7	26487		ACIS-S	14.88	2022-08-07
C8	25782		ACIS-S	30.66	2023-01-29
C9	25780		ACIS-S	11.92	2023-06-16
C10	25779		ACIS-S	19.82	2023-07-04
C11	25778		ACIS-S	19.81	2023-07-04
C12	25781		ACIS-S	13.60	2023-07-18
XM3	0943790101		EPIC	104.20	2025-07-08
F606W	j8r331010		ACS/WFC	0.68	2003-08-03
F814W	j8r331020		ACS/WFC	0.70	2003-08-03
F606W	jc9104010		ACS/WFC	2.40	2014-01-21
F814W	jc9104020		ACS/WFC	2.53	2014-01-21
NGC 1097					
CH1	2339		ACIS-S	5.34	2001-01-28
CH2	1611		ACIS-S	5.34	2001-01-28
XMM1	922490201		EPIC	33	2023-12-22
CH3	30142		ACIS-S	9.94	2025-05-21
CH4	30937		ACIS-S	9.94	2025-05-21
CH5	30938		ACIS-S	9.94	2025-05-21
CH6	29637		ACIS-S	14.71	2025-05-31
CH7	30948		ACIS-S	14.71	2025-05-31
F814W	j8mx03fsq		ACS/WFC	0.12	2004-06-05
F336W	icc501021		WFC3/UVIS	1.43	2014-02-20
F438W	icc501041		WFC3/UVIS	0.81	2014-02-20
F814W	icc501050		WFC3/UVIS	0.70	2014-02-20
F814W	jdxk38010		ACS/WFC	2.15	2019-05-28
F275W	idxr58040		WFC3/UVIS	2.3	2020-08-14
F555W	idxr58030		WFC3/UVIS	2.30	2020-08-14
F115W	jw03707		NIRCam/IMAGE	0.22	2023-12-27
F115W	jw04793		NIRCam/IMAGE	0.86	2024-09-29
F200W	jw04793		NIRCam/IMAGE	0.86	2024-09-29
F300M	jw03707		NIRCam/IMAGE	0.22	2023-12-27
F335M	jw03707		NIRCam/IMAGE	0.86	2023-12-27
F335M	jw04793		NIRCam/IMAGE	1.63	2024-09-29
F360M	jw04793		NIRCam/IMAGE	1.63	2024-09-29
F444W	jw04793		NIRCam/IMAGE	1.63	2024-09-29
F277W	jw04793		NIRCam/IMAGE	0.86	2024-09-29

Notes: NGC 4631, with Target IDs 00082263 and 00084441, was observed 24 times between 2013-11-08 and 2021-02-13. For NGC 1097 ULX-3, we analyzed 84 *Swift*/XRT PC observations (Target ID 00045597, 2011 Aug 05–2025 Jun 06) and 2 additional observations (Target ID 00036582, 2007 Aug 02–Dec 16).